

## Observations and modeling of steep-beach grain-size variability

A. J. H. M. Reniers,<sup>1</sup> E. L. Gallagher,<sup>2</sup> J. H. MacMahan,<sup>3</sup> J. A. Brown,<sup>3</sup> A. A. van Rooijen,<sup>4,5</sup> J. S. M. van Thiel de Vries,<sup>4,5</sup> and B. C. van Prooijen<sup>5</sup>

Received 20 March 2012; revised 24 September 2012; accepted 6 November 2012; published 4 February 2013.

[1] Novel observations of surface grain-size distributions are used in combination with intra-wave modeling to examine the processes responsible for the sorting of sediment grains on a relatively steep beach (slope = 1:7.5). The field observations of the mean grain size collected with a digital camera system at consecutive low and high tides for a 2 week period show significant temporal and spatial variation. This variation is reproduced by the modeling approach when the surf zone flow-circulation is relatively weak, showing coarse grain sizes at the location of the shore break and finer sediment onshore and offshore of the shore break. The model results suggest that grain size sorting is dominated by the wave-breaking-related suspended sediment transport which removes finer sediment from the shore break and transports it both on-shore and offshore. The transport capacity of wave-breaking-related suspended sediment is controlled by the sediment response time scale in the advection-diffusion equation, where small (large) values promote onshore (offshore) transport. Comparisons with the observed beach profile evolution suggest a relatively short time scale for the suspended sediment response which could be explained by the vigorous breaking of the waves at the shore break.

**Citation:** Reniers, A. J. H. M., E. L. Gallagher, J. H. MacMahan, J. A. Brown, A. A. van Rooijen, J. S. M. van Thiel de Vries, and B. C. van Prooijen (2013), Observations and modeling of steep-beach grain-size variability, *J. Geophys. Res. Oceans*, 118, 577–591, doi:10.1029/2012JC008073.

### 1. Introduction

[2] In the past, hydrodynamic and morphologic coastal modelers have usually assumed that the sand layer on a beach is thick, well sorted (uniform in grain size), and relatively smooth. However, many recent studies contradict this assumption and show that not only grain size varies with location on the beach but also heterogeneity in grain size may play a role in determining morphology and its dynamics [e.g., Gallagher *et al.*, 1998; Ruessink *et al.*, 2007]. For example, both Richmond and Sallenger [1984] and Stauble and Cialone [1997] observed an inverse depth dependency for the grain size distribution (coarser in shallower water, with the coarsest material at the shore break) at Duck, North Carolina, with coarsening of the bed material during storm conditions due to an offshore directed transport of finer material.

[3] The shore break is typically characterized by a sudden increase in the steepness of the bottom profile at the offshore edge of the swash zone with intense plunging wave breaking. The corresponding rotational flow is able to trap surf zone material including swimmers (J. A. Battjes, personal communication). Once caught in the shore break, it can be difficult to find your footing and get out. The violent wave action leads to a collection of relatively coarse bed material at the shore break, with finer material both offshore and onshore of the shore break. The morphodynamic relevance of this coarse layer has been inferred from numerical modeling by Ruessink *et al.* [2007] who replaced the bed at the shore break with a fixed layer within their bar-evolution modeling studies. Without this fixed layer, their simulations ended prematurely following unrealistic erosion of the steep foreshore; hence, the shore break potentially exerts a strong morphological control on the beach profile evolution. Note that the position of the shore break is not necessarily fixed but can vary with the tidal elevation, provided the waves are strong enough to move the coarse material up and down the beach as observed on a gravel beach [Buscombe and Massellink, 2006].

[4] To model the formation and evolution of a shore break, the temporal and spatial evolution of the grain size distribution as function of the (changing) local wave and flow conditions is required. Variable grain size modeling has been performed in the past to examine its effects on sediment transport [e.g., Guillen and Hoekstra, 1996], stratigraphy of deltas [Geleynse *et al.*, 2010], and tidal channels [Dastgheib *et al.*, 2009]. Here we propose to use

<sup>1</sup>Rosenstiel School of Marine and Atmospheric Science, University of Miami, Miami, Florida, USA.

<sup>2</sup>Franklin and Marshall College, Lancaster, Pennsylvania, USA.

<sup>3</sup>Naval Postgraduate School, Monterey, California, USA.

<sup>4</sup>Deltares, Delft, The Netherlands.

<sup>5</sup>Delft University of Technology, Delft, The Netherlands.

Corresponding author: A. J. H. M. Reniers, Applied Marine Physics, Rosenstiel School of Marine and Atmospheric Science, University of Miami, 4600 Rickenbacker Causeway, Miami, FL 33149, USA. (areniers@rsmas.miami.edu)

© 2012 American Geophysical Union. All Rights Reserved.  
2169-9275/13/2012JC008073

a one-dimensional (1D) multi-grain-size transport and bed-evolution model to examine the formation of a shore break made up of relatively coarse material forced by tidally modulated sea-swell incident waves. To verify the model, we compare with observations of bottom profiles and concurrent temporal and spatial grain size distributions obtained during the 2009 rip current exchange (REX) field experiment at Sand City, Monterey Bay, CA.

[5] Traditional grain size measurements require collection of samples from the field site, transport to the laboratory, and subsequent preparation and analyses resulting in a tedious and time consuming process. This traditional routine for collecting grain size information is especially cumbersome if many samples are needed to resolve detailed spatial and temporal variations. Here a newly developed technique was used to facilitate the collection of high spatial and temporal resolution grain size information from digital images [Gallagher *et al.*, 2011].

[6] These unique measurements in combination with a novel intra-wave morphodynamic model will allowed us to investigate the processes responsible for the temporal and spatial variations of the grain size distribution in the swash zone. This is a first step in understanding the morphodynamic feedback of grain size variability on beach profile evolution.

## 2. REX Field Observations

[7] The rip current exchange experiment (REX) at Sand City was performed in two consecutive parts during the spring of 2009. Here we focus on the first part of the experiment ranging from yeardays 120 to 131. During the experiment, the intertidal grain size distribution was digitally mapped at high and low tide at two neighboring cross-shore transects. The N-array is aligned with the rip channel at  $Y=90$  m, and the S-array is located at  $Y=110$  m, 20 m above the N-array (Figure 1). During the experiment, the shoals are pushed onshore creating feeder channels at either side of the center rip channel as can be inferred from the two panels in Figure 1.

[8] The corresponding intertidal bottom profiles at the S- and N-arrays show moderate variation during the experiment (Figures 2a and 2b) with a mean slope in the order of 1:7.5 obtained from the alongshore averaged profiles (Figure 2c). The observed variability in the individual profiles is either associated with the formation and propagation of beach cusps (around  $x=25$  m, Figure 1) or the migration of mega cusps [Orzech *et al.*, 2010, 2011] coupled to the rip-and-feeder channels (around  $x=55$  m, Figure 1). Averaging over the rip-channel spacing, this variability is removed, showing minimal changes in the swash zone bed profiles for the duration of the experiment (Figure 2c).

[9] During the REX experiment, the semi-diurnal tidal excursion increased from a neap tide (day 122) to a spring tide (day 129) (dark blue line, Figure 3a). In addition, there is significant variation about the semi-diurnal tidal elevation owing to waves during the first part of the REX experiment measured with the pressure sensors located in the S-array (Figure 3a). This also can be seen in the difference between the offshore wave height measured with CDIP buoy 156 ([www.cdip.ucsd.edu](http://www.cdip.ucsd.edu)) and the local wave height (Figure 3b). At the start of the experiment, the incident waves correspond to moderate swell with a root mean square wave height of about 1 m and a mean wave period of 10 s. Around the middle of yearday 126, more energetic swell waves arrive increasing the offshore wave height to approximately 2 m. In subsequent days, the wave height tapers down to  $O(1)$  m again with a concurrent increase in the mean wave frequency related to increased contribution of sea waves at this time. The wave incidence angle at Sand City is close to shore normal during this time (not shown). At times of high waves and low tides, the rip-current circulation is at its strongest as expressed by the Froude number,  $F_r$  (Figure 3c), calculated at the rip-ADCP located at approximately 2.5 m water depth (Figure 1). Froude numbers of  $O(0.1)$  thus correspond to a rip current velocity of approximately 0.5 m/s [MacMahan *et al.*, 2006].

[10] The cross-shore distribution of the mean surface grain size was digitally measured from macrophotographs

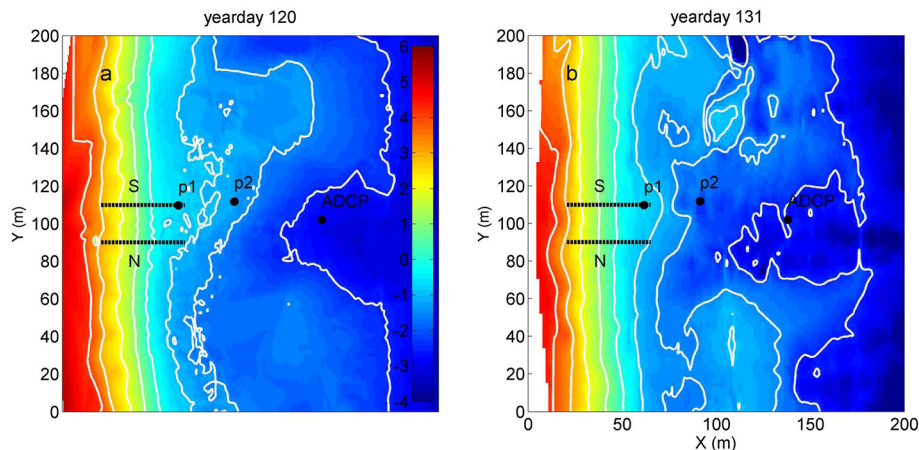


**Figure 1.** REX surveys on yeardays 120 (a) and 131 (b) with bed levels in m indicated by the color bar in Figure 1a. Locations of the N- and S-cross-shore arrays are indicated by the dashed black lines. Locations of pressure sensors p1 and p2 and rip-located Acoustic Doppler Current Profiler (ADCP) indicated by the black dots. Bottom contours at  $[-2.5 \ -1.5 \ -1 \ 0 \ 1 \ 2 \ 3 \ 4]$  m as a reference (white lines).

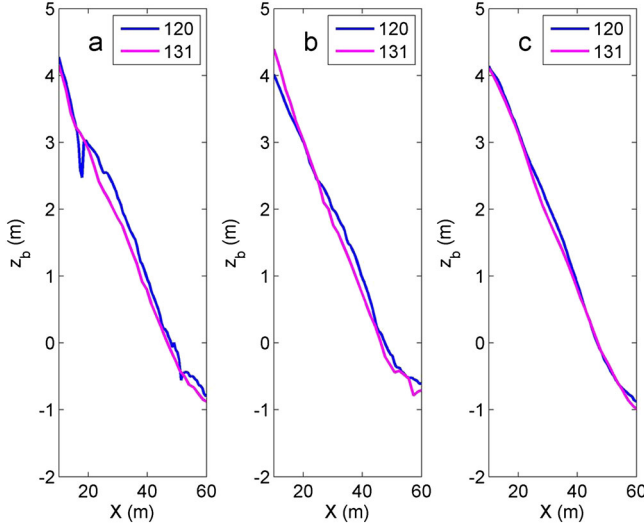


**Figure 2.** Cross-shore profiles measured during REX at yeardays 120 and 131. (a) Profiles at S-array. (b) Profiles at N-array. (c) Alongshore averaged profiles.

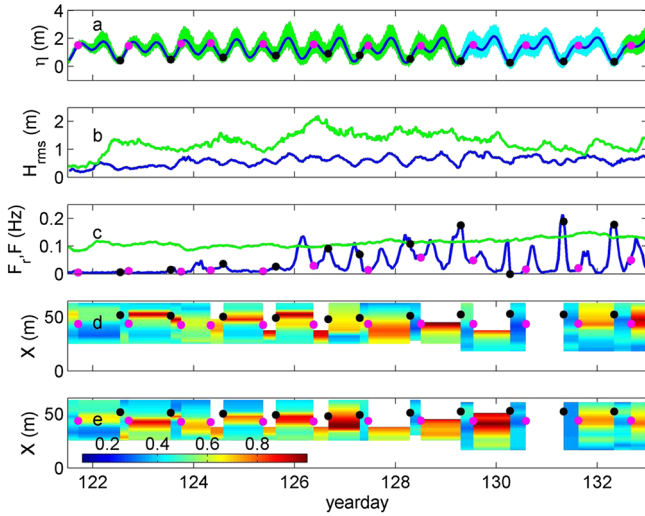


**Figure 3.** (a) Water surface elevation relative to the bed measured at p1 (green) and p2 (cyan), respectively. Half-hour-averaged elevation corresponding to the tidal elevation indicated by the blue line. (b) Root mean square wave height measured by the p1/p2 pressure sensors (blue) and offshore wave height measured by CDIP 156 (green). (c) Froude number for rip current flow within the rip channel (blue) at the ADCP location. Mean frequency of the incident waves (green) measured by the ADCP. (d) Observations of cross-shore median grain-size distribution,  $D_{50}$ , in millimeter at high tide (after pink dot) and low tide (after black dots) along the intertidal beach at the S-array. (e) Similar for the N-array. Note that grain size surveys were done at the time marked by dots but are extended for the whole time between surveys to aid in visualization.

of beach sand obtained with an off-the-shelf camera and underwater housing during both low and high tide during daylight hours, producing Digital Imaging System (DIS)

estimates that have been shown to correlate highly with estimates from sieves ( $R^2=0.92$ ) [Gallagher *et al.*, 2011]. Due to the semi-diurnal character of the tide, the tidal elevation during the time of observation does not necessarily correspond to the lowest/highest tidal elevation of that day (Figure 3a). The general result showed a coarser grain size distribution in the vicinity of the shore break (Figures 3d and 3e) consistent with the observations of Stauble and Cialone [1997] and Guillen and Hoekstra [1996]. However, as the shore break moves up and down the shoreface with the tide, the coarse patch also moves up and down the beach. At high tide, the observations are frequently incomplete due to the vigorous wave breaking which prevented the DIS operation (Figures 3e and 3d).

[11] After yearday 128, the tidal range reached its maximum (Figure 3a) with energetic waves (Figure 3b). At this time, the mean surface grain size showed large variations within a tidal cycle; coarse grains during the high tide and relatively fine grains without an apparent shore break or coarse patch during the low tide (Figure 3d and 3e). These observations coincide with a strong rip current circulations (Figure 3c) and are potentially related to the strong along-shore variation in the rip current flow velocities [MacMahan *et al.*, 2010] and concurrent sediment transport during these times [Roelvink and Reniers, 2011].

[12] In summary, there is a visible correlation between the cross-shore distribution of the mean surface grain size and the position of the shore break as inferred from the tidal elevation, provided the rip-current circulation is weak. In the presence of strong rip currents, there is no apparent maximum at low tide, displaying a more uniform distribution of relatively fine sediments. During the course of the experiment, the changes in alongshore averaged swash bed profiles are minimal, implying a balance in the cross-shore sediment transport. As mentioned earlier, the incident waves during the experiment were predominantly normally incident, and the littoral swash transports are consequently expected to be insignificant compared with the cross-shore transports. In the following, we will use these observations to verify a hydrostatic swash model and examine the sediment transport processes responsible for grain size sorting.

### 3. Sediment Transport Processes

[13] Sand within the swash zone is transported by the combined wave and flow motions, where bottom shear stress, wave asymmetry, and skewness as well as wave-breaking-induced turbulence are important [Beach and Sternberg, 1996, Puleo *et al.*, 2000; Butt *et al.*, 2004]. The water depth changes from approximately zero to tens of cm during each wave cycle and the sediment response to these extreme fluid changes is consequently rapid. Swash zone sediment transport is facilitated by gravity operating along the bed during the back wash. Conversely, transport is inhibited by gravity operating along the bed during the uprush. These bed-slope effects become more important for increasing profile steepness and are assumed to balance excess onshore transport leading to an equilibrium beach slope [Dean, 1973].

[14] Masselink and Hughes [1998] found good agreement with observed transport rates using both an energetics-based [Bagnold, 1963, 1966] and a shear-stress-related sediment transport model [Meyer-Peter and Muller, 1948] provided



that the calibration coefficients used for the up rush were twice as large compared with those used for the backwash. The need for an enhanced calibration factor suggests that some processes are not (well) represented in both the energetics- and shear-stress-based sediment transport models.

[15] One process that is likely to be important in the swash is the fluid acceleration. Variation in the thickness of the bottom boundary layer leads to an asymmetric shear stress distribution for a harmonic wave, which can be accounted for by including the fluid acceleration in calculating the shear stress [Nielsen, 1992, Nielsen and Callaghan, 2003, Terrile et al., 2009]. In effect, the fluid acceleration by means of the corresponding pressure gradient exerts a force on the particles [Drake and Calantoni, 2001] which contributes to the sediment transport [Hoefel and Elgar, 2003]. For large pressure gradients, the upper sediment bed layer can become unstable and move as a block [Madsen, 1975, Foster et al., 2006].

[16] Another important transporting mechanism is intense wave breaking-induced turbulence. Visual inspection at the beach shows that at the onset of wave breaking at the shore break, large amounts of sediment are transported from the bed into the breaking wave. This suspended sediment is subsequently transported up the beach slope by the breaking wave with vigorous stirring by the bore-related turbulence. Butt et al. [2004] used an energetics-based model extended with wave-breaking-induced turbulence and found an O(10)% improvement in the agreement with observed ensemble averaged sediment transport rates. However, the results obtained by Butt et al. [2004] were obtained in relatively deep water due to the required submergence of the ADV, and wave-breaking events were relatively sparse. By selecting only wave breaking events, an O(50)% improvement was obtained, indicating a significant contribution by breaking related turbulence to swash zone sediment transport. The inclusion of the breaker-related turbulent stirring in the inner swash zone also explained the very high time-averaged suspended sediment concentrations observed for longer period waves simulating extreme storm conditions in the Delta flume [van Thiel de Vries et al., 2008].

[17] Ground water flow is another process that can be of importance. During the up rush, water infiltrates the sand causing a stabilizing effect, whereas during the backwash, water exfiltrates the sand pushing the sand up. These effects are typically small for sand ( $D_{50} < 0.45$  mm) but become important for coarser sediment [Turner and Masselink, 1998]. This process is not considered here.

## 4. Model Description

### 4.1. Introduction

[18] Modeling of sediment transport within the swash zone has received considerable attention in the recent past, ranging from relatively simple empirical models to very sophisticated models solving the Navier Stokes equations (NSE) (see Bakhtyar et al. [2009] for an extensive review). The objective here is to model the mean grain size distribution and morphological change over a period of 10+ days. This makes the application of NSE-models unsuitable due to their large computational effort, and the relatively simple empirical models do not have all the necessary transport processes. Given the fact that  $k_w h$ , with  $k_w$  representing the

wave number and  $h$  the instantaneous water depth, is small for all free surface gravity waves considered within the swash (i.e., incident wind waves, swell and infra-gravity waves), the corresponding flow motion will be solved using the non-linear shallow water equations (NLSWE). This is not the case for the turbulent motions associated with wave breaking, and these are therefore not resolved by the present modeling approach but calculated with a simplified depth-averaged turbulent kinetic energy balance instead (discussed later). This approach is in line with Kobayashi and Johnson [2001] and Alsina et al. [2009], whom combined the NLSWE with a simplified turbulent kinetic energy balance and an advection-diffusion equation to describe suspended sediment transport in the swash zone. In addition to their approach, bed load sediment transport is included as well as the grain-size dependent sediment response and stratigraphy required to simulate grain size sorting as observed by the DIS.

### 4.2. Hydrodynamics

[19] In the following, a 1D version of the XBeach model [Roelvink et al., 2009] solving the NLSWE is used to resolve the intra-wave swash fluid motions and concurrent sediment transport. The NLSWE-1D continuity equation and cross-shore momentum equation are given by

$$\frac{\partial \eta}{\partial t} + \frac{\partial hu}{\partial x} = 0, \quad (1)$$

$$\frac{\partial u}{\partial t} + u \frac{\partial u}{\partial x} - \nu_h \left( \frac{\partial^2 u}{\partial x^2} \right) = -\frac{\tau_{bx}}{\rho_w h} - g \frac{\partial \eta}{\partial x}, \quad (2)$$

where  $h$  is the total water depth including the wave related surface elevation,  $\eta$ ,  $u$  is the velocity in the  $x$  direction positive onshore,  $\tau_{bx}$  is the cross-shore bed shear stress,  $g$  is the gravitational acceleration,  $\rho_w$  is the water density, and  $\nu_h$  is the horizontal turbulent eddy viscosity. The bottom shear stress is calculated from the instantaneous velocity and a friction factor

$$\tau_{bx} = \rho_w c_f |u| u, \quad (3)$$

where the friction coefficient is given by

$$c_f = \frac{g}{C^2}, \quad (4)$$

and  $C$  represents the Chezy coefficient. Comparisons with the laboratory observations of Ting and Kirby [1994] for plunging breaking waves on a slope show a good match with the surface elevation and intra-wave velocities (section A). Additional model comparisons by van Rooijen et al. [2012] using the intra-wave swash Truc Vert field observations collected and described by Blenkinsopp et al. [2011] further support the present approach.

### 4.3. Turbulence Model

[20] Wave breaking is defined by wave fronts that exceed a critical slope,  $m_{cr}$ . This spatial criterion is translated into a time-dependent threshold by assuming that the wave front propagates with  $\sqrt{gh} + u$ :

$$\frac{\partial \eta_{cr}}{\partial t} = m_{cr} (\sqrt{gh} + u). \quad (5)$$

The change in bore thickness,  $R$ , is then calculated from

$$\frac{\partial R}{\partial t} = \left[ \max \left[ \frac{\partial \eta}{\partial t}, 0 \right] - \frac{\partial \eta_{cr}}{\partial t} \right]. \quad (6)$$

[21] The source term related to the dissipation of the organized wave energy is subsequently obtained from

$$S_w = c_R R g \frac{\partial \eta_{cr}}{\partial t}, \quad (7)$$

and the dissipation of turbulent kinetic energy,  $k$ , is given by

$$S_r = c_k k^{\frac{3}{2}}, \quad (8)$$

where  $c_R$  and  $c_k$  are calibration coefficients. This completes the depth-averaged turbulent energy transport equation

$$\frac{\partial kh}{\partial t} + \frac{\partial kh u}{\partial x} = S_w - S_r. \quad (9)$$

[22] To account for the vertical decay of the turbulence with distance from the surface, an exponential decay function has been added [Roelvink and Stive, 1989]:

$$k_{bed} = k \min \left( \frac{1}{\exp \left( \frac{h}{R} \right) - 1}, 1 \right), \quad (10)$$

where  $R$  is the roller thickness calculated from equation (6). The turbulent kinetic energy balance is a simplified description ignoring many of the complicated generation, transport, and dissipation mechanisms in the presence of intense breaking waves but including the intra-wave turbulence response required for the phase-coupled breaking-induced sediment transport. Hence, prior to the sediment transport calculations, a comparison is made with the detailed laboratory experiments of *Ting and Kirby* [1994] to constrain the turbulence model parameters, showing a reasonable match with the observed intra-wave near-bed turbulence (section A). The turbulence will be used in the following to calculate the bed load and suspended load sediment transport described below.

#### 4.4. Sediment Transport Model

[23] The bed load transport in the intra-wave model is calculated with the shear-stress of *Nielsen* [2006] based on the model of *Meyer-Peter and Muller* [1948]:

$$S_b = 12 \beta_s \left[ \max \left[ |\theta'(t)| - \theta_{cr}, 0 \right] \right] \sqrt{\theta'(t)} \frac{u(t)}{|u(t)|} \sqrt{\Delta g D^3}, \quad (11)$$

where  $u(t)$  is the instantaneous cross-shore velocity,  $D$  is the grain size diameter, and  $\theta_{cr}$  is a threshold value of the non-dimensional shear stress that has to be exceeded for the initiation of motion. The presence of near-bed turbulence increases the bed shear stress under oscillatory waves analogous to the enhanced current shear stress in the presence of waves [Fredsoe et al., 2003]. As a first-order approximation of this process, the non-dimensional shear stress,  $\theta'$ , given by the Shields number [Shields, 1936] is enhanced with

the near-bed wave-breaking related turbulent stirring in the following way:

$$\theta'(t) = \frac{0.5 f_{2.5} (u^2(t) + k_{bed})}{g \Delta D} \quad (12)$$

where  $f_{2.5}$  is the wave friction factor given by *Swart* [1974]:

$$f_{2.5} = \exp \left( 5.213 \left( \frac{2.5D}{A} \right)^{0.194} - 5.977 \right), \quad (13)$$

and  $A$  is the excursion. The wave-related friction factor for the cross-shore flow velocity is included to represent the boundary layer effects associated with the oscillatory character of the swash. The relative weight of the sand is given by

$$\Delta = \frac{(\rho_s - \rho_w)}{\rho_w}, \quad (14)$$

with  $\rho_s$  the density of sand.

[24] Finally, the bed-slope correction factor is given by

$$\beta_s = \cos \beta_b \left( 1 - \frac{u(t)}{|u(t)|} \frac{\tan \beta_b}{\tan \phi} \right), \quad (15)$$

where  $\phi$  is a critical bed slope and  $\beta_b$  is the local bed slope. This factor inhibits upslope transport and facilitates downslope sediment transport.

[25] To account for boundary layer effects in the bed shear stress, *Nielsen* [1992] introduced a phase shift  $\phi_t$  in the near bed velocities to calculate the shear stress velocities at the bed:

$$u_*(t) = \sqrt{0.5 f_{2.5}} \left( \cos(\varphi_t) u(t) + \sin(\varphi_t) \frac{1}{\omega_{rep}} \frac{\partial u(t)}{\partial t} \right), \quad (16)$$

where  $\omega_{rep}$  is a representative radial wave frequency which corresponds to the mean period of the incident waves. The fluid acceleration in the model is obtained from a running average

$$\frac{\partial u(t)}{\partial t} \simeq \frac{1}{T_a} \int_{t-T_a}^t \left[ \frac{u(\tilde{t}) - u(\tilde{t} - \delta t)}{\delta t} \right] d\tilde{t}, \quad (17)$$

where  $\delta t$  is the numerical time step and  $T_a$  is 0.5 s.

[26] The depth-averaged equilibrium suspended sediment concentration associated with wave breaking only is calculated according to *Roelvink and Stive* [1989] based on the energetics approach of *Bagbold* [1963, 1966]:

$$c_{eq} = \frac{\epsilon_s k_{bed}^{\frac{3}{2}}}{w_s}, \quad (18)$$

where  $w_s$  is the sediment fall velocity calculated according to *Ahrens* [2000] and  $\epsilon_s$  is the suspended load efficiency [Baillard, 1981]. The suspended sediment transport is modeled with a depth-averaged advection-diffusion equation [Galappatti and Vreugdenhil, 1985]:

$$\frac{\partial hc}{\partial t} + \frac{\partial hc u}{\partial x} + \frac{\partial}{\partial x} \left[ K h \frac{\partial c}{\partial x} \right] = \frac{hc_{eq} - hc}{T_s}, \quad (19)$$

where  $c$  represents the instantaneous depth-averaged sediment concentration and  $K$  is the horizontal diffusivity coefficient set equal to the turbulent eddy viscosity,  $v_h$ , given by

$$v_h = \max(0.1, 0.3h\sqrt{k}), \quad (20)$$

with  $k$  the turbulent kinetic energy calculated from equation (9). The vertical entrainment of the sediment is represented by an adaptation time,  $T_s$ , given by a simple approximation based on the local water depth and sediment fall velocity [Reniers *et al.*, 2004]:

$$T_s = \max\left(\gamma \frac{h}{w_s}, 0.01\right), \quad (21)$$

where  $\gamma$  is a calibration factor and a small value of  $T_s$  corresponds to nearly instantaneous sediment response. This approach ignores depth-dependent phase lags between sediment concentration and fluid flow. The cross-shore suspended sediment transport is thus given by

$$S_s = hcu + Kh \frac{\partial c}{\partial x}, \quad (22)$$

[27] To model grain size effects, XBeach has been extended with multiple sediment classes. In this multi-grain-size module, a thin active layer of 2 cm with sediment of varying grain sizes is readily available for transport in combination with a 10 cm thick transition layer followed by a large number of underlying passive layers of 10 cm thickness. In the case of erosion, sediment is extracted from the transition layer and the thickness of the transition layer decreases accordingly. With continued erosion, the transition layer thickness goes to zero and the underlying passive layer is activated. In the case of accretion, the thickness of the transition layer increases until the thickness exceeds 10 cm after which a new transition layer is created and the old transition layer becomes passive.

[28] Both the suspended and bed load transports are affected by grain size variability as outlined below. In the following, each sediment class represents a grain size diameter and corresponding fall velocity calculated according to Ahrens [2000]. Based on the fractions of the various sediment classes present in the top layer, the suspended equilibrium concentration per sediment class,  $j$ , can be expressed as follows:

$$c_{eq}(j) = p(1,j) \frac{I_s k_{bed}^3}{w_s(j)}, \quad (23)$$

where the index 1 refers to the top layer and  $p$  represents the fraction of a specific sediment class within that layer. Next, the advection-diffusion equation, equation (19), is solved independently for the different sediment classes leading to class dependent suspended sediment transport rates,  $S_s(j)$ . The offshore boundary condition for the suspended sediment concentration is given by

$$c_0(j) = \max[c_{eq,0}(j), c_{\delta x}(j)]. \quad (24)$$

[29] The bed load transport for each sediment class is calculated according to equation (11), multiplied by the fraction of available sand for each sediment class within the top layer:

$$S_b(j) = p(1,j) 12\beta_s \left[ \max[|\theta'(j,t)| - \theta_{cr}, 0] \right] \sqrt{\theta'(j,t)} \frac{u(t)}{|u(t)|} \sqrt{\Delta g D(j)^3}, \quad (25)$$

from which the bottom changes per sediment class can be derived (see section B). Mixture effects such as armoring [e.g., Wiberg *et al.*, 1994] and diffusion have not been taken into account. The bed level at the offshore boundary is fixed over a distance of 5 grid points assuming it is kept in place by inner surf zone processes including rip current circulations that are not represented by the model. This also means that the grain size distribution at these locations does not change in time.

#### 4.5. Model Implementation

[30] The XBeach model is applied in a 1D cross-shore setting with a constant grid size of 1.5 m spanning 63 m. The time step is automatically calculated based on the requirement that the Courant number is less than one. The Riemann boundary offshore absorbs the reflected incident waves prescribed by the surface elevation measured by pressure sensor p1 (see Figure 1). A Chezy number,  $C$ , of  $65 \text{ m/s}^{0.5}$  corresponds to a friction coefficient of 0.0023 (equation (4)), representative of waves breaking on a planar beach [Garcez Faria *et al.*, 1998]. The turbulence and roller model parameters are based on a comparison with the laboratory experiments of Ting and Kirby [1994] (section A). The turbulence sediment stirring coefficient,  $\epsilon_s = 0.008$ , is obtained by comparing the predicted morphological evolution with the profile observations and is close to the value of 0.01 used by Bagnold [1966]. The adaption time calibration factor,  $\gamma$ , is obtained by comparing with the DIS-observed mean grain size variability. The bed load transport parameter,  $\phi_t = 40^\circ$ , is adopted from the study by Nielsen and Callaghan [2003]. The relevant model parameters are summarized in Table 1 and are kept constant throughout the numerical simulation. More details on the numerical implementation of the wave, flow, and sediment transport equations can be found in Roelvink *et al.* [2009], van Rooijen [2011], and van Rooijen *et al.* [2012].

#### 5. Model Results

[31] The model hindcast period covers a 10 day period from yearday 122 through 132. This period includes a number of tides and changes in the incident wave conditions (Figure 3). The initial profile for the model calculations corresponds to the alongshore averaged profile surveyed on yearday 120 (Figure 2c). Between yearday 120 and the start of 122, the root mean square wave heights were less than 0.25 m and it is assumed that this led to minimal changes in the bottom profile. The initial sediment grain size distribution in the model assumes an equal fraction for each of these grain sizes, [0.1 0.2 0.3 0.4 0.5 0.65 0.8 0.95 0.12 15] mm, in all 10 layers. This initial distribution is based on a post-experiment sieving analysis of sand samples collected along

**Table 1.** Model Parameter Settings

$C \text{ (m/s}^{0.5}\text{)}$	$c_k$	$c_R$	$m_{cr}$	$\gamma$	$\omega_{rep} \text{ (rad/s)}$	$A \text{ (m)}$	$\epsilon_s$	$\phi_t^\circ$
65	0.4	0.4	0.07	0.1	0.63	10	0.008	40



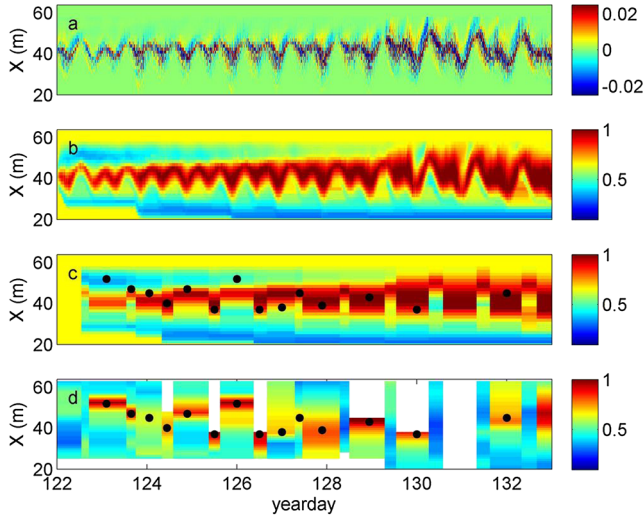


**Figure 4.** (a) Calculated bed elevation changes in 10 min intervals for a 9 day period (color scale in m). (b) Predicted cross-shore distribution of  $D_{50}$  (color scale in millimeter). (c) Predicted cross-shore distribution of  $D_{50}$  at the same times as the DIS observations shown in (d) (color scale in mm). Locations of maximum  $D_{50}$  in DIS-observed cross-shore distributions are indicated by black dots.

the two cross-shore DIS-sampling transects (Figure 1) and thus represents all grain sizes available over the whole beach.

[32] The computed bottom changes within the swash zone show strong intermittency with seemingly randomly

distributed erosive and accretive events (Figure 4a) as discussed by *Blenkinsopp et al.* [2011]. As a consequence, the net inter-tidal bathymetric change is typically small although gross changes are large. This suggests that large amounts of sand are moving in the swash, which is important for grain sorting, where coarse and fine fractions can be moving, while the overall bathymetry is not changing.

[33] The predicted spatial distribution of grain sizes at the bed surface is similar to the observations with significantly coarser material in the vicinity of the shore break, located around  $x \sim 40$  m, accompanied by finer material both onshore and offshore of the shore break. The modeled  $D_{50}$  spatial surface distribution establishes itself within one tidal cycle (likely owing to the large gross transport), and the coarse region shows a smooth onshore/offshore motion with the rising and falling tide (Figure 4b). Because the observations were made at high and low tides only, the predicted profiles are sub-sampled at the times of the DIS observations and plotted like the observations in Figure 3d (reproduced in Figure 4d). Comparing Figures 4c and 4d, both the magnitude of the mean grain size (color scale) and the cross shore position of the maximum grain size (dots) exhibit a good correspondence between model and observations during high tide. During low tide, there is good correspondence provided the rip circulation is weak (Figure 3c, yeardays 122–126 showing black dots with low Froude numbers). The lower skill during low tides occurs predominantly during times of strong rip current circulations.

[34] Snapshots of profile change and grain size redistribution as the model progresses are shown in Figure 5.

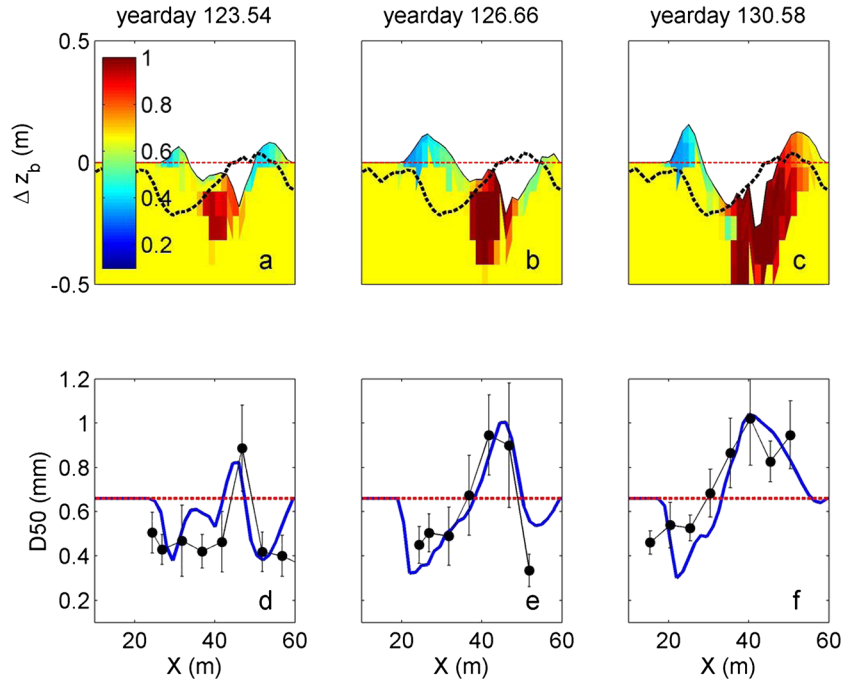


**Figure 5.** Snapshots of predicted profile changes (with respect to the initial profile on yearday 120) and corresponding  $D_{50}$  (in millimeter indicated by the color bar) grain size at an early high tide (a), a low tide (b), and a late high tide (c) during the 10 day period. For reference, measured profile changes between yearday 120 and 131 are indicated by the dashed black line. Comparisons between predicted (blue lines) and N-S transect-averaged DIS-observed surface grain size (black lines) with corresponding standard deviations indicated by the vertical bars at an early high tide (d), a low tide (e), and a late high tide (f). The modeled initial  $D_{50}$  grain size profile is indicated by the red dashed line.

The model predicts the coarsening of  $D_{50}$  at the shore break (located at  $x \sim 40$  m) and the fining of the surface sediments both on- and offshore of the shore break (Figures 5a–5c). The computed surface  $D_{50}$  grain size profile during these snapshots of high and low tides during the 10 day period shows a good comparison with the observations (Figures 5d–5f) with model predictions almost always within the DIS-observed uncertainty band width. These snapshots are typical (at least while Froude numbers are low) and encouraging.

[35] The black dashed lines in Figures 5a–5c indicate the observed profile change for the model period (yeardays 120–131). The predicted profile changes are of the same order as the observed profile change both in magnitude and in shape, with erosion near the shore break of about 30 cm and accretion both onshore and offshore of 10–20 cm. Note that the model is capable of maintaining the cross shore beach profile over a 10 day period using constant parameter settings (Table 1). The step in the modeled bed elevation at the shore break is consistent with visual observations at the field site. The mismatch between the observed and predicted profile change (Figure 5c) shows a moderate over-prediction of the erosion (of 10–20 cm) at the middle of the intertidal zone and accompanying over-prediction of accretion at both the high tide and low tide areas. Based on the model-data comparison, we conclude that the model has significant skill in predicting time-varying and spatially varying surface grain size within the intertidal zone on a steep beach.

## 6. Grain Size Sorting Processes

[36] The first 2 h of the model simulation is analyzed in more detail to examine the processes responsible for the grain size sorting. At this time, the tidal elevation is +1.2 m and the  $H_{rms} = O(0.4)$  m (Figure 3). Calculating the mean and standard deviation of the cross-shore velocity  $u$  and turbulent velocity  $\sqrt{k_{bed}}$  shows that the means are of similar order but the standard deviation is larger for  $u$  than  $\sqrt{k_{bed}}$  (compare Figures 6a and 6b). The cross-shore velocities are at a maximum at the shore break and have stronger offshore components than onshore, resulting in a mean offshore directed current. The maxima in the turbulent and wave-related velocities occur around the shore break after which they rapidly decay in the onshore direction. The turbulent velocities also decay in the offshore direction as the water becomes deeper, because not all waves are breaking at this location and the vertical attenuation, equation (10), increases with depth. The corresponding mean surface elevation (with the tide removed) shows a small set-down at the shore break followed by a wave-induced setup in the surf/swash zone. The surface elevation standard deviation shows the shoaling up to the shore break followed by a rapid decrease towards the shore.

[37] The corresponding bed load transport is offshore directed at the shore break (Figure 6d). Farther offshore, at  $x \sim 45$  m the bed load sediment transport drops off quickly and is onshore directed, due to the positive phase shift in the shear velocity, equation (16). This effect is somewhat

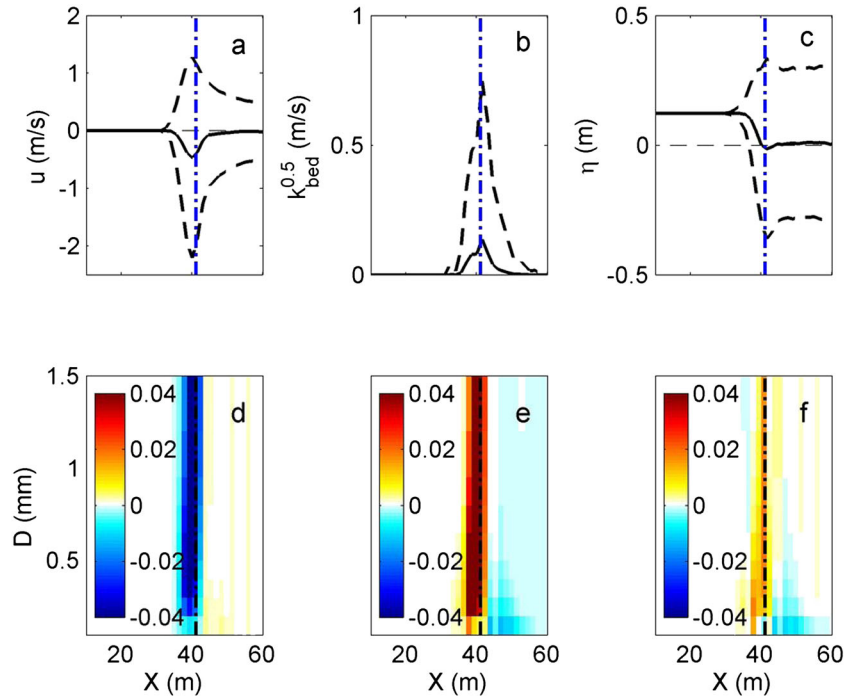


**Figure 6.** Model simulations of the first 2 h of yearday 122. (a) Mean cross-shore flow velocity (solid line) plus or minus 2 times the standard deviation (thick dashed lines). (b) Mean turbulent velocity (solid line) plus 2 times the standard deviation (dashed line). (c) Mean water level setup without the tidal elevation (solid line) plus 2 times the standard deviation of the surface elevation (tick dashed lines). (d) Grain-size-dependent time-averaged bed load sediment transport. (e) Grain-size-dependent time-averaged suspended load sediment transport. (f) Combined bed load and suspended load sediment transports in  $m^2/h$ . Approximate shore break position is indicated by the dash-dotted line. Velocity and transport are positive in the onshore direction.



stronger for the finer sediments. In contrast, the suspended load sediment transport (Figure 6e) is predominantly onshore directed at the shore break. Beyond  $x \sim 45$  m, the suspended sediment is transported offshore with higher transport rates for the finer grain sizes. Combining the bed load and suspended load transport (Figure 6f), the net sediment transport shows a convergence of coarser material ( $D > 1$  mm) in the vicinity of the shore break and concurrent divergence of finer sand ( $D < 0.5$  mm). Also, under these conditions, relatively more fine sediments are removed from the shore break near  $x \sim 40$  m resulting in a coarsening of the remaining material.

[38] To examine grain-size-dependent transport in more detail, calculations for 1 m water depth are used. The bed load sediment transport calculations show that for free stream velocities less than about 1 m/s, more fine sediment is transported for a given flow velocity than coarse sediment (Figure 7a). This is intuitive and due to the fact that the critical shear stress inhibits the sediment motion for larger grain size particles. However, this relationship is not linear (Figure 7b). The steep dropoff in  $\theta$  with increasing grain size diameter is a result of the  $D^2$  dependence of the drag force mobilizing the particle and the  $D^3$  dependence of the

stabilizing gravitational force leading to an inverse dependence of  $\theta$  with  $D$  (equation (12)) thereby favoring transport of finer material at lower velocities. However, at higher velocities, transport of coarser grains is actually slightly dominant.

[39] In the field case, offshore of the shore break, where velocities are lower, the bed load sediment transport is dominated by the finer grain sizes (Figure 6d). If the Shields number  $\theta$  is less than the critical Shields number, sediment is not mobilized at all. The corresponding area of zero transport is shown in Figure 7a. For free stream velocities larger than 1 m/s, the effect of the critical shear stress is weak and as a result the bed load sediment transport is larger for the larger grain sizes as the frictional drag, equation (13), increases with grain size. This explains the predominance of larger grain size bed load sediment transport at the shore break where velocities can easily exceed 2 m/s (Figure 6a).

[40] Adding near bed turbulence to the calculation of the Shields number has a significant effect on the initiation of motion, as nearly all grain sizes are now mobilized, but a relatively small influence on the bed load transport of large sediment sizes for free stream velocities larger than 1 m/s (compare Figures 7a and 8a).

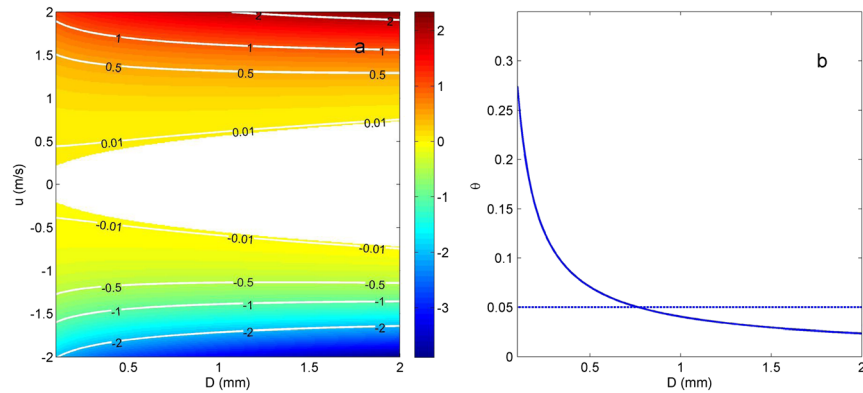


**Figure 7.** (a) Bed load sediment transport at 1 m water depth as function of the cross-shore velocity and grain size diameter without wave breaking turbulence. No sediment particle motion is indicated by the white area. Color bars and contour lines represent sediment transport in  $\text{m}^2/\text{h}$ . (b) Shields stress for a free stream velocity of 0.5 m/s as function of grain size diameter. The critical Shields stress that needs to be exceeded to mobilize the sediment is indicated by the horizontal dashed line. Transport is positive in the onshore direction.

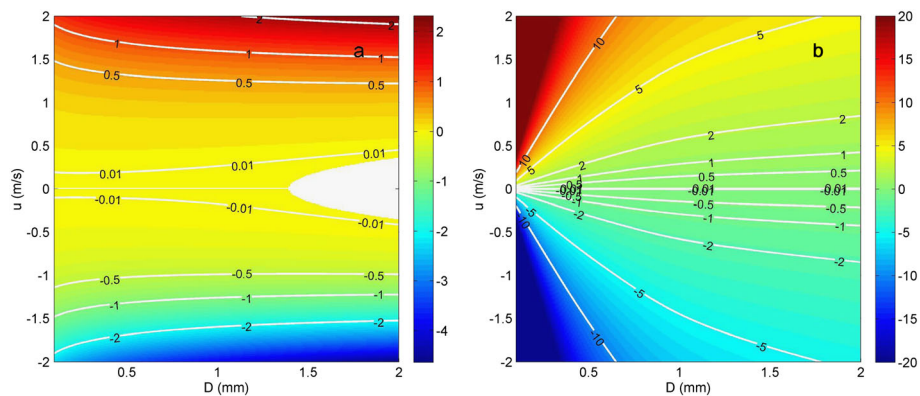


**Figure 8.** (a) Bed load sediment transport as function of the free stream velocity and grain size diameter at 1 m water depth with  $0.4 \text{ m}^2/\text{s}^2$  wave breaking turbulence added. (b) Suspended load sediment transport for  $0.4 \text{ m}^2/\text{s}^2$  wave breaking turbulence at 1 m water depth ignoring diffusion. Color bars and contour lines represent sediment transport in  $\text{m}^2/\text{h}$ . Transport is positive in the onshore direction.

[41] The suspended sediment transport is evaluated by multiplying the equilibrium suspended sediment concentration due to breaking induced turbulence with the free stream velocity and local water depth ignoring diffusive effects:  $S_s = h c_{eq} u$  (compare with equation (22)). Due to the inverse dependence of the suspended sediment equilibrium concentration, equation (23), on the sediment fall velocity (Figure 9), the suspended transport is dominated by fine material (Figure 8b).

[42] As the turbulent bore travels with the wave front, the suspended sediment transport is expected to be predominantly onshore directed. However, the actual transport will be determined by the phase lag between the suspended sediment concentration and the cross-shore velocity as dictated by the advection-diffusion equation, equation (19). This response time scale  $T_s$ , equation (21), is inversely proportional to the fall velocity. As a consequence, the fine material that is brought into suspension by the breaking-induced turbulence will linger in the water column and will be subject to the mean offshore directed flow (Figure 6a). This explains why the finest suspended sediment is transported offshore (Figure 6e). As the fall velocity increases, this effect diminishes and the suspended sediment concentration peak caused by the breaking wave turbulence becomes in phase with the onshore velocity of the breaking wave crest resulting in onshore transport. With increasing grain size, less sand is mobilized by breaking induced turbulence (Figure 9b) resulting in decreasing transports of larger fractions for a given cross-shore velocity. This explains why unlike the bed load sediment transport, the suspended sediment transports are biased towards smaller grain sizes (Figure 6e).

[43] Separating the fine and coarse (at  $D_{50} = 0.65$  mm) sediment transport and concomitant bed elevation changes for the 2 h computation initialized at the beginning of yearday 122 shows that there is a small onshore flux of finer sediment that is deposited near the waterline shoreward of the shore break. There is also a larger offshore flux of finer sediment that is collected offshore (Figure 10). The eroded coarser material is deposited at the shore break, replacing the finer material, resulting in a layer of relatively coarse sediment at the shore break around  $x \sim 40$  m. The preferential removal of fine sand leads to a further coarsening in the

vicinity of the shore break. These results support the findings of *Stauble and Cialone* [1997] and the present observations. This response can be explained by the relatively short suspension time of the coarse material resulting in a short transport distance whereas the finer material is moved farther offshore as it lingers in the water column. The inflection points in the surface  $D_{50}$  profile (Figure 10b) coincide with the intersection points of the fine and coarse material transports (Figure 10c). These grain size sorting processes are found to be robust where the initial deposition of finer material onshore and offshore of the shore break is accompanied by a relative increase in the amount of coarser material in the vicinity of the shore break. This pattern persists through many tidal cycles and wave conditions consistent with the observations (Figure 4).

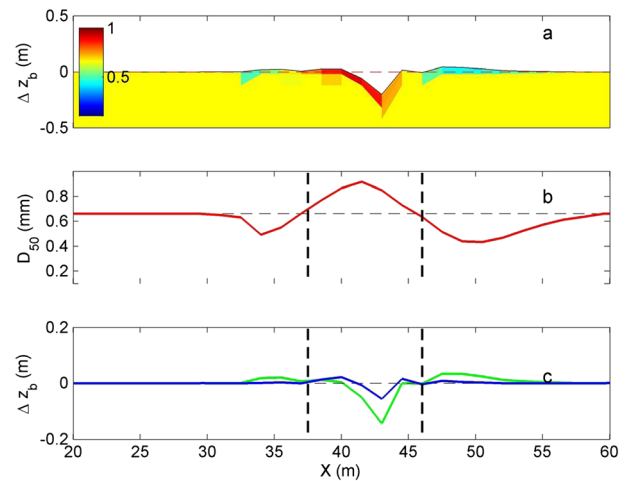


**Figure 10.** (a) Computed  $D_{50}$  spatial distribution and bed elevation changes after 2 h initialized at yearday 122. Color scale represents  $D_{50}$  in millimeter. (b) Surface  $D_{50}$  profile (solid red line), with the initial  $D_{50}$  profile given by the black dashed line. (c) Computed bed level changes for fine sediment with  $D_{50} \leq 0.65$  mm (green line) and coarse sediment with  $D_{50} > 0.65$  mm (blue line). The locations of bed elevation change that are equal for both grain size groups are indicated by the vertical dashed lines.

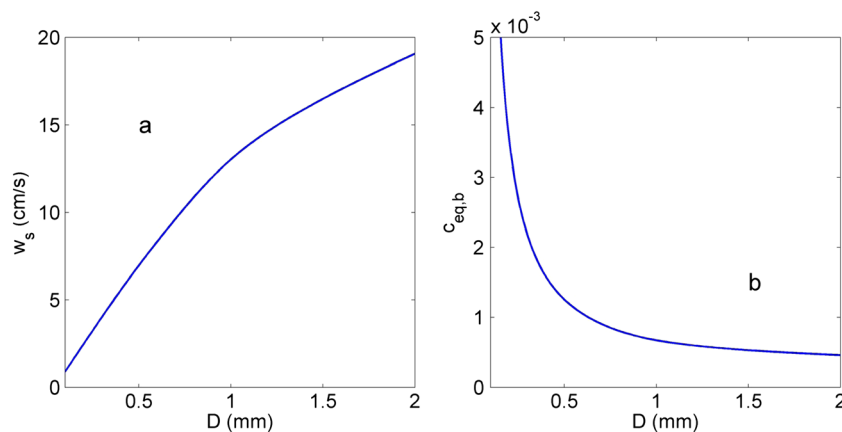


**Figure 9.** (a) Sediment fall velocity as function of grain size diameter calculated with *Ahrens* [2000]. (b) Equilibrium suspended sediment concentration for a near bed wave breaking turbulence value of  $0.4 \text{ m}^2/\text{s}^2$  using equation (23).

## 7. Discussion

[44] In the following, we examine the initial morphodynamic response (calculated for a 2 h duration starting at yearday 122) and the sensitivity to different transport processes and parameter settings. Excluding the suspended sediment transport from the calculations results in erosion onshore of the shore break, near the waterline (Figure 11a), and a buildup of sand offshore of the initial shore break position. For a prolonged calculation, this leads to significant erosion of the beach profile that is not supported by the observations (not shown). The differences in fine and coarse sediment transport are relatively small resulting in small changes in the surface  $D_{50}$  distribution (Figures 11b and 11c).

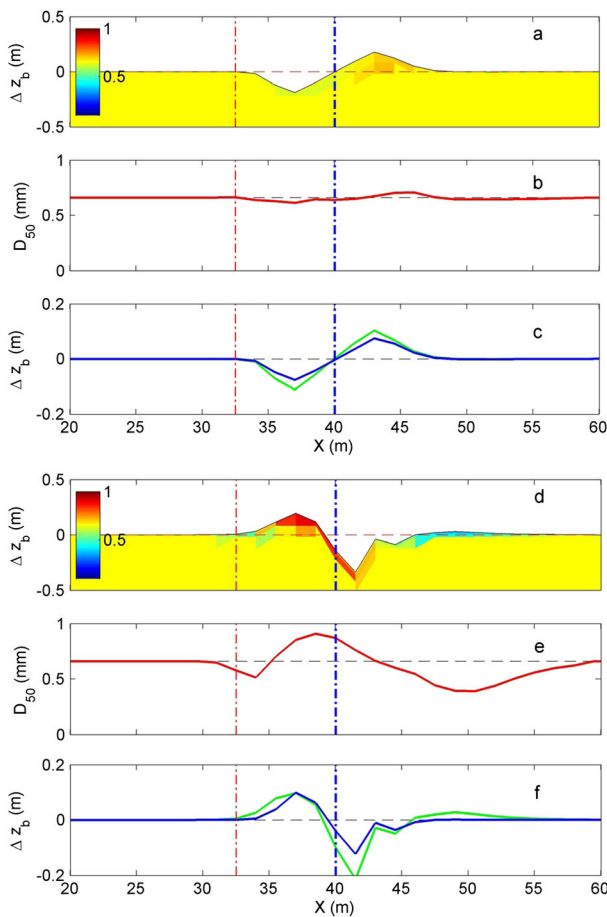


**Figure 11.** (a) Computed  $D_{50}$  spatial distribution and bed elevation changes after 2 h calculated with bed load only, initialized at yearday 122. Color scale represents  $D_{50}$  in millimeter. (b) Surface  $D_{50}$  profile (solid red line) calculated with bed load only. The initial  $D_{50}$  profile is given by the black dashed line. (c) Computed bed level changes calculated with bed load only, for fine sediment with  $D_{50} \leq 0.65$  mm (green line), and coarse sediment with  $D_{50} > 0.65$  mm (blue line). (d–f) are the same as (a–c), respectively, but calculated with suspended load sediment transport only. In all panels, the approximate locations of the shore break (vertical blue dashed line) and waterline (vertical red dashed line) are given as a reference.

[45] This result contrasts with the case without the bed load contribution which leads to an accretion of sediment near the waterline as sediment is eroded from the shore break area (Figure 11d). For prolonged calculations, this leads to a large accumulation of sediment near the waterline, which is also not supported by the observations. Relatively more fine sediment is removed from the shore break (Figure 11f) resulting in coarsening of the surface material (Figure 11e). The subsequent deposition of coarse grain size material shoreward of the shore break occurs sooner than the deposition of finer material resulting in strong cross-shore modulation of the  $D_{50}$  distribution. Consistent with the full computation, the finest material is moved offshore resulting in a smaller  $D_{50}$  offshore of the shore break.

[46] These results suggest that both bed load and suspended load are needed to create the observed changes of the bed and the observed patterns in spatial distribution of surface sediment grain size.

[47] Next, we examine the role of the suspended sediment response time scale by setting  $\gamma$  to a value of 0.5 (where  $\gamma = 0.1$  in the earlier calculations and a higher  $\gamma$  results in a longer time spent in the water column). This leads to erosion and coarsening at the shore break as more material and a large fraction of fine material are removed and only coarse material remains behind (Figure 12a). The eroded sediment is predominantly deposited offshore of the shore break, it extends slightly farther offshore, and it contains a slightly larger fraction of coarse sediment (represented by a larger  $D_{50}$  offshore of the shore break, compare Figures 12b and 10b). At the waterline, only the coarsest sediment remains as evidenced by the shoreward shift and larger peak in the  $D_{50}$  profile (compare Figures 12b and 10b). The slower sediment response thus reduces or removes the onshore transport capacity of the breaking waves (compare Figures 12c and 10c) as the sediment stays in the water column longer and transport becomes dominated by the offshore directed mean flow resulting in increasing advection distances with decreasing grain size diameters. Decreasing the response time scale  $T_s$  by setting  $\gamma$  to 0.01, which corresponds to an almost instantaneous sediment response for the suspended sediment, results in erosion of the bed in the vicinity of the shore break and subsequent deposition near the waterline (Figure 12d). Also, the bed material becomes coarser at the shore break and finer near the shore line, consistent with the observations. However, it cannot explain the presence of fine material observed offshore, as there is no deposition offshore of the shore break for  $\gamma = 0.01$  (Figure 12f).

[48] The optimal  $\gamma$  value of 0.1 is significantly smaller than the value of 0.3 used by *Gallappatti and Vreugdenhil* [1985] for coarse sediment. This is most likely the result of the injection of turbulence by breaking waves accompanied by vigorous turbulent mixing within the water column. This process is expected to have much shorter vertical mixing time scales than the sediment response associated with the flow velocity considered by *Gallappatti and Vreugdenhil* [1985], which in turn can lead to asymmetric adaption times [*Roelvink and Reniers*, 2011], and is a topic that requires more research.

[49] Finally, we examine the role of the phase shift in the near bed velocity used to calculate the bed shear stress and accompanying bed load transport. Differences for  $\phi_t = 0^\circ$  and  $\phi_t = 40^\circ$  are small and the changes in  $D_{50}$  distribution



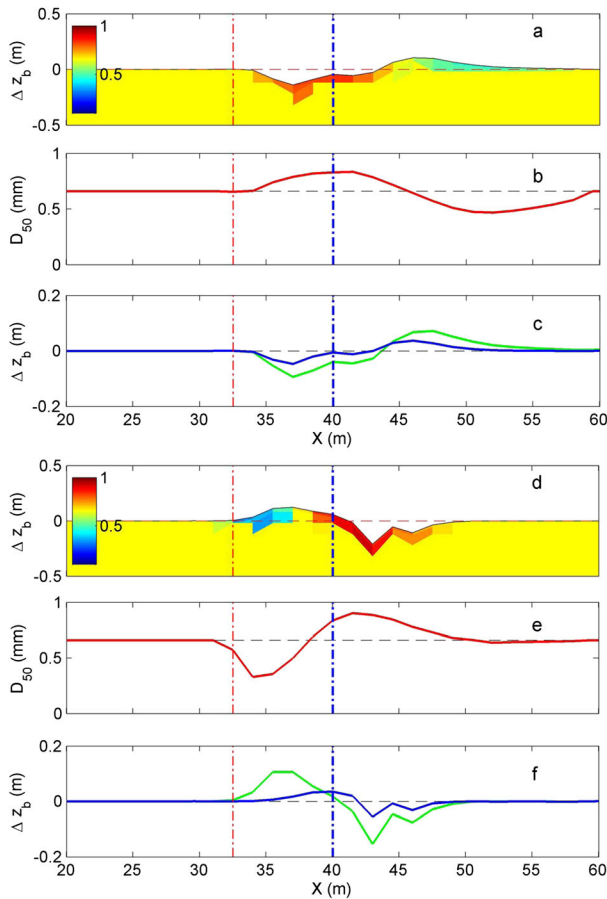


**Figure 12.** (a) Computed grain size distribution and bed elevation changes after 2 h without bed load sediment transport and longer time scale  $T_s$  with  $\gamma = 0.5$  initialized at yearday 122.0 with uniform grain size distribution. Color scale represents  $D_{50}$  in millimeter. (b) Surface  $D_{50}$  grain size distribution (solid red line). The corresponding initial distribution is given by the black dashed line. (c) Computed bed level changes for fine sediment with  $D_{50} \leq 0.65$  mm (green line) and coarse sediment with  $D_{50} > 0.65$  mm (blue line). (d–f) Same as Figures 12a–12c but with shorter time scale  $T_s$  by setting  $\gamma$  to 0.01. Approximate locations of the shore break (vertical blue dashed line) and waterline (vertical red dashed line) are given as a reference.

appear negligible over the course of 2 h (not shown). Thus, the phase-lag effect of the near-bed velocity appears small at these time scales but may still be important for long-term beach profile development.

[50] Model predictions start with an initially uniform distribution (equal amounts of each size class) and thus ignore any pre-existing stratigraphy. The fact that the model predictions give a fair match with the observations suggests that the time scales associated with grain size sorting at the bed surface of the profile are rapid and that the cross-shore spatial grain size patterns are robust with moderate and dynamic changes associated with tidal elevation and incident wave conditions.

[51] Unfortunately, the present instrument setup does not allow for a proper separation of incident and reflected waves

at the offshore model boundary. As a result, the incident wave energy is overestimated in the present modeling approach. Analysis of the ADCP measurements shows a frequency-dependent reflection coefficient ranging from 0.9 for the infra-gravity waves and 0.2 for the shorter sea waves. Reducing the incident wave energy at the offshore model boundary based on these reflection estimates showed minimal changes in the predicted profile change and surface grain size spatial patterns, showing that this is a robust feature of the modeling approach.

[52] The observations used here for model-data comparisons do not include measurements of turbulent velocities, suspended sediment transports, nor bed load transports. However, *van Rooijen* [2011] and *van Rooijen et al.* [2012] show that the calculated sediment transports with this model are representative of the detailed swash observations at Truc Vert described by *Blenkinsopp et al.* [2011], including intra-wave sediment transport rates and bed-elevation changes. In addition, the turbulence model has been verified and constrained with the laboratory experiments from *Ting and Kirby* [1994] (although this does not account for scale effects which can be important). Instead of direct comparisons with data, observed profile changes are used, thus requiring that the combined suspended and bed load transport is able to simulate the observed sorting and profile changes. The main objective of the study is to explain the grain size sorting observed on many natural beaches. To this end, the model results are robust.

## 8. Conclusions

[53] Novel observations of grain-size variability on a steep (1:7.5) beach obtained with a digital camera system show significant modulation with both the tidal elevation changes and wave and flow conditions. The shore break, defined as the area of vigorous wave breaking is characterized by a region of coarse sediment, which appears to remain in place as finer material is transported both onshore and offshore of the shore break by swash processes. These observations in combination with bathymetric surveys have been used to verify an intra-wave model based on the shallow water equations. The model includes a variable grain size routine that allows for the independent transport of different sediment size fractions. In addition, the model includes a heuristic description of the wave breaking induced turbulence, which is important at the shore break.

[54] Based on the model results, we conclude that the combined suspended and bed load transport contributions are required to maintain the beach profile and to explain the cross-shore observed spatial distribution of sediment on the surface. A key parameter in dispersing the sediment and maintaining the beach profile is the phase lag effect resulting from a balance between fall velocity and turbulence in the water column, which is expressed by the sediment response time scale  $T_s$  [*Gallapatti and Vreugdenhil*, 1985]. Model results suggest that this time scale is relatively small consistent with a near-instantaneous sediment response at the shore break and consistent with the results obtained by *Reniers et al.* [2004] and *van Rooijen et al.* [2012]. Both model simulations and observations suggest that the changes in spatial distribution of the grain size occur rapidly on intra-tidal time scales.

## 9. Turbulence Model Comparison

[55] To constrain the simplified wave-breaking-induced turbulence description, equations (5)–(10), a comparison is made with the laboratory experiments of *Ting and Kirby* [1994]. This choice is based on the fact that their intra-wave ensemble-averaged laboratory experiments are performed under controlled conditions and field observations of intense wave-breaking-induced turbulence are notoriously difficult and erratic [e.g., *George et al.*, 1994, *Voulgaris and Collins*, 2000, *Aagaard and Hughes*, 2010]. The use of small-scale laboratory experiments does introduce scale effects that are not accounted for. The numerical model is set up to simulate the swash zone flows for their regular plunging wave condition with a wave period of 5 s and an offshore wave height of 12.8 cm on a constant bottom slope of 1:35 (see *Ting and Kirby* [1994] for details of their experimental setup). The surface elevation envelope is well predicted, showing the presence of non-linear waves with somewhat higher crests and flatter troughs (Figure A1a). This is confirmed by a comparison with the observed saw-tooth shaped surface elevation at  $X=10.3$  m (Figure A1b). The corresponding velocities also compare well (Figure A1c), supporting the present hydrostatic description of intra-wave swash (equations (1)–(4)). Satisfactory results for the turbulent kinetic energy are obtained by setting the source and sink parameters,  $c_R$  and  $c_k$  (in equations (7) and (8)), to 0.4, mimicking the sharp increase in near-bed turbulent kinetic energy that is phase-coupled with the steep front of the breaking wave (Figure A1d). This means that only part of the roller energy; i.e., 40% is transformed into small-scale turbulence within the water column [e.g., *Feddersen and Trowbridge*, 2005]. The turbulent decay

coefficient of 0.4 is consistent with the  $O(1)$  estimate by *Roelvink and Stive* [1989]. The trailing edge in the measured turbulence is not represented by the simplified model description as the delayed arrival of turbulence by obliquely descending eddies is not accounted for. Although this is not expected to have a large impact on the net-sediment transport, as the elevated turbulence occurs for both positive and negative wave velocities, further study is warranted.

## 10. Sediment Grain Size and Bed Updating

[56] The bed is discretized into layers with mass  $M(i,j)$ , in which  $i$  refers to the layer number and  $j$  to the sediment class. The mass fraction per sediment class  $p$ , layer thickness  $\Delta z$ , and bed level  $z_b$  are defined by

$$p(i,j) = \frac{M(i,j)}{\sum_{j=1}^J M(i,j)}$$

$$\Delta z(i) = \frac{1}{(1-n_p)\rho_s} \sum_{j=1}^J M(i,j)$$

$$z_b = z_0 + \sum_{i=1}^I \Delta z(i),$$

with porosity  $n_p$  and sediment density  $\rho_s$ . The Level  $z_0$  is the lowest point of the array of bed layers.

[57] Due to bed load transport, sediment is exchanged between the top layer and the two horizontally neighboring top layers. Exchange with the water column and the top layer is due to erosion rate,  $E$ , and deposition rate,  $D$ . A

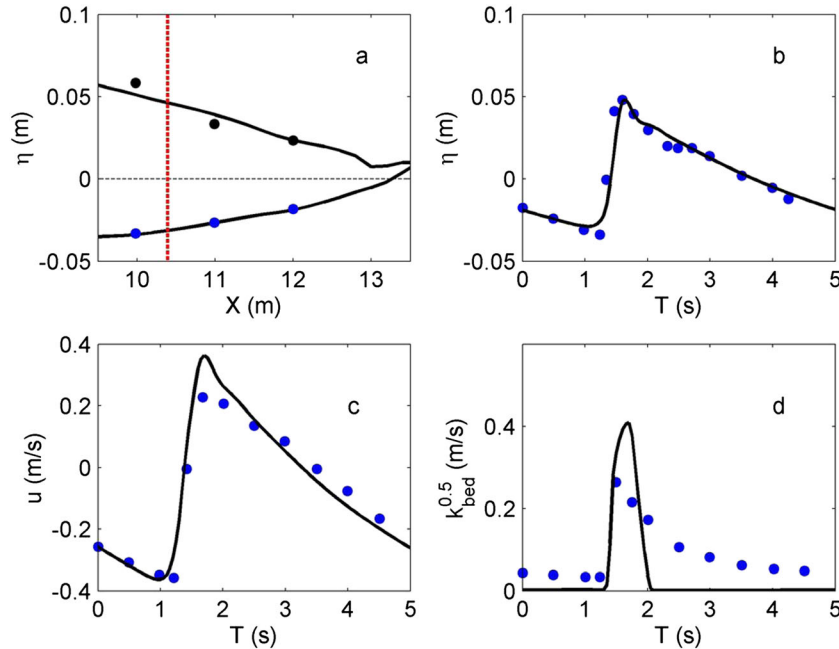


**Figure A1.** (a) Computed surface elevation envelope (solid line) compared with observations (dots). (b) Model (black line) comparison with the intra-wave surface elevation (dots) at  $X=10.3$  (indicated by the vertical red dashed line in Figure A1a). (c) Comparison of model (black line) and observed (dots) velocities at  $X=10.3$  m. (d) Comparison of model (black line) and observed (dots) turbulent near-bed kinetic energy at  $X=10.3$  m.

mixed Eulerian/Lagrangian framework is proposed. Within the set of layers, one layer is defined as the variable layer. This is the only layer that has a variable total mass. All other layers have a constant total mass, which implies for a constant porosity a constant thickness. Above the variable layer, the layers move with the bed level (Lagrangian): upwards in case of aggradation and downwards in case of degradation. This vertical movement gives an advective flux with advection velocity equal to the bed level change,  $N = \frac{\partial z}{\partial t}$ . The variable layer is the transition to the lower layers, which are passive. The number of layers below the variable layer has thus no influence on the computation time. Note that diffusive processes within the bed are not considered here.

[58] The mass balance for the top layer can now be defined by

$$\frac{\partial M(1,j)}{\partial t} = dx\{p(1,j)S_b(j)\}_U - dx\{p(1,j)S_b(j)\}_D - dxp(1,j)E(j) + dxD(j) + dx\delta Np_{bot}(1,j)$$

$$N = \sum_{j=1}^J \left\{ dx\{p(1,j)S_b(j)\}_U - dx\{p(1,j)S_b(j)\}_D - dxp(1,j)E(j) + dxD(j) \right\}$$

[59] The mass balance for the layers in between the top layer and the variable layer is

$$\frac{\partial M(i,j)}{\partial t} = dxA(p_{bot}(i,j) - p_{ceil}(i,j)),$$

and for the variable layer, it reads

$$\frac{\partial M(i,j)}{\partial t} = Np_{ceil}(i,j),$$

[60] In order to avoid too thin or too thick a variable layer, the variable layer is merged or split. If the thickness is smaller than the critical value,  $\Delta z_{merge}$ , the variable layer is merged with the lower layer. To keep the same number of cells, a cell is added at the bottom of the array, implying that  $z_0 = z_0 - \Delta z$ . Similarly, the variable is split into two layers if the critical value  $\Delta z_{split}$  is exceeded. Then the array is shifted upwards:  $z_0 = z_0 + \Delta z$ .

[61] As the bed level update is explicit, the time step is limited. A conservative estimate can be made by assuming that no more mass can be eroded than available in the top layer:

$$dx\{p(1,j)S_b(j)\}_{U/D} + dxp(1,j)E(j) < \frac{M(1,j)}{dt},$$

and

$$dt < \frac{(1 - n_p) \rho_s \Delta z(1)}{S_{b,U/D}(1) + E(1)}.$$

[62] The transport rate depends on the direction of the transport. The transport rates and erosion rates should be based on the formulation for the smallest fraction:  $j = 1$ . Note that the fraction  $p$  falls out. This time step restriction is less severe than the one for shallow water flow. Only in case of very thin top layers and/or the use of a morphological factor, this time step restriction might be relevant. In the present modeling effort, the layer below the top layer was acting as the variable layer.

[63] **Acknowledgments.** This work was funded by Deltares-Rijkswaterstaat Coastal Maintenance Research Program Kustlijnzorg, the National Science Foundation grants, and the Office of Naval Research Coastal Geosciences grants. AR was funded through NSF grant EAR0952225 and ONR grant N000140710556. EG was funded through NSF grants EAR0952164 and OCE0340758 and ONR grant N000140510153. JM was funded through NSF grants EAR-0952182 and OCE-0926750 and ONR grants N0001409WR20221 and N0001409WR20222. Friends and colleagues who also helped enormously include Ian Smithgall, Clement Gandon, Ron Cowen, Keith Wycoff, and Ed Thornton.

## References

- Aagaard, T., and M. C. Hughes (2010), Breaker turbulence and sediment suspension in the surf zone, *Marine Geol.*, **271**, 250–259.
- Ahrens, J. P. (2000), The fall-velocity equation, *J. Waterw. Port Coastal Ocean Eng.*, **126** (2), 99–102.
- Alsina, J. M., I. Caceres, J. Sospedra, and T. E. Baldock (2009), *J. Coastal Res.*, **56**, 1716–1720.
- Bagnold, R. A. (1963), Mechanics of marine sedimentation. In: *The Sea*, 3. Hill, M. N. (Ed.) Wiley Interscience, NY, 507–528.
- Bagnold, R. A. (1966), An approach to the sediment transport problem from general physics. US Geological Survey Professional Paper 422–I, 37.
- Bailard, J. A. (1981), An energetics total load sediment transport model for a plane sloping beach, *J. Geophys. Res.*, **86**, 10,938–10,954.
- Bakhtyar, R., D. A. Barry, L. Li, D. S. Jeng, and A. Yeganeh-Bakhtiary (2009), Modeling sediment transport in the swash zone: A review, *Ocean Eng.*, **36**, 767–783.
- Beach, R. A., and R. W. Sternberg (1996), Suspended sediment transport in the surf zone: Response to breaking waves, *Cont. Shelf Res.*, **16**, 1989–2003.
- Blenkinsopp, C. E., I. L. Turner, G. Masselink, and P. R. Russell (2011), Swash zone sediment fluxes: Field observations, *Coastal Eng.*, **58** (1), 28–44.
- Buscombe, D., and G. Masselink (2006), Concepts in gravel beach dynamics, *Earth Sci. Rev.*, **79** (1–2), 33–52.
- Butt, T. P., Russell, J. Puleo, J. Miles, and G. Masselink (2004), The influence of bore turbulence on sediment transport in the swash and inner surf zones, *Cont. Shelf Res.*, **24**, 757–771.
- Dastgheib, A., J. A. Roelvink, and M. Van der Wegen (2009), Effect of different sediment mixtures on the long term morphological simulation of tidal basins, in *Proc. RCEM* (Santa Fe, Argentina), 913–918.
- Dean, R. (1973), Heuristic models of sand transport in the surf zone, in *Proc. of Conference on Engineering Dynamics in the Surf Zone* (Sydney, Australia Institution of Engineers), 208–214.
- Drake, T. G., and J. Calantoni (2001), Discrete particle mode for sheet flow sediment transport in the nearshore, *J. Geophys. Res.*, **106** (C9), pp. 19859–19868.
- Feddersen, F., and J. H. Trowbridge (2005), The effect of wave breaking on surf-zone turbulence and alongshore currents: A modeling study, *J. Phys. Oceanogr.*, **35**, 2187–2203.
- Foster, D. L., A. J. Bowen, R. A. Holman, and P. Natoo (2006), Field evidence of pressure gradient induced incipient motion, *J. Geophys. Res.*, **111**, C05004.
- Fredsoe, J., B. M. Sumer, A. Kozakiewicz, L. H. C. Chua, and R. Deigaard (2003), Effect of externally generated turbulence on wave boundary layer, *Coastal Eng.*, **49**, 155–183.
- Gallagher, E. L., S. Elgar, and R. T. Guza (1998), Observations of sand bar evolution on a natural beach, *J. Geophys. Res.*, **103**, 3203–3215.
- Gallagher, E. L., J. H. MacMahan, A. J. H. M. Reniers, J. A. Brown, and E. B. Thornton (2011), Grain size variability on a rip-channelled beach, *Mar. Geol.*, **287**, 43–53.
- Galappatti, R., and C. Vreugdenhil (1985), A depth integrated model for suspended transport, *J. Hydraul. Res.*, **23** (4), 359–377.
- Garcez Faria, A. F., E. B. Thornton, T. P. Stanton, C. V. Soares, and T. C. Lippmann (1998), Vertical profiles of longshore currents and related bed shear stress and bottom roughness, *J. Geophys. Res.*, **103** (C2), 3217–3232.
- Geleynse, N., J. E. A. Storms, M. J. F. Stive, H. R. A. Jagers, and D. J. R. Walstra (2010), Modeling of a mixed-load fluvio-deltaic system, *Geophys. Res. Lett.*, **37**, L05402, doi:10.1029/2009GL042000.
- George, R., R. E. Flick, and R. T. Guza (1994), Observations of turbulence in the surf zone, *J. Geophys. Res.*, **99**, 801–810.
- Guillen, J., and P. Hoekstra (1996), The “equilibrium” distribution of grain size fractions and its implications for cross-shore sediment transport: A conceptual model, *Mar. Geol.*, **135**, 15–33.
- Hoefel, F. G., and S. Elgar (2003), Wave-induced sediment transport and sandbar migration, *Sci.*, **299** (1), 1885–1887.



- Kobayashi, N., and B. D. Johnson (2001), Sand suspension, storage, advection, and settling in surf and swash zones, *J. Geophys. Res.*, **106** (C5), 9363–9376.
- MacMahan, J. H., E. B. Thornton, and A. J. H. M. Reniers (2006), Rip current review, *Coastal Eng.*, **53**, 191–208.
- MacMahan, J. H., J. Brown, J. Brown, E. B. Thornton, A. J. H. M. Reniers, T. P. Stanton, M. Henriquez, E. Gallagher, J. Morrison, M. J. Austin, T. M. Scott, and N. Senechal (2010), Mean Lagrangian flow behavior on an open coast rip-channeled beach: A new perspective, *Mar. Geol.*, **268** 1–4, 1–15.
- Madsen, O. (1975), Stability of a sand bed under breaking waves, in *Proc. 14th Int. Conf. Coastal Eng.* (Copenhagen, Denmark), pp. 776–794.
- Masselink, G., and M. Hughes (1998), Field investigation of sediment transport in the swash zone, *Cont. Shelf Res.*, **18**, 1179–1199.
- Meyer-Peter, E. R., and Muller (1948), Formulas for bed-load transport, in *Proc. of the 2nd Meeting of the International Association for Hydraulic Structures Research*, Delft, The Netherlands, 39–64.
- Nielsen, P. (1992), Coastal bottom boundary layers and sediment transport. Advanced Series on Ocean Engineering, World Scientific, Singapore, **4**, 324.
- Nielsen, P., and D. P. Callaghan (2003), Shear stress and sediment transport calculations for sheet flow under waves, *Coastal Eng.*, **47**, 347–354.
- Nielsen, P. (2006), Sheet flow sediment transport under waves with acceleration skewness and boundary layer streaming, *Coastal Eng.*, **53**, 749–758.
- Orzech, M. D., E. B. Thornton, J. H. MacMahan, W. C. O'Reilly, and T. P. Stanton (2010), Alongshore rip channel migration and sediment transport, *Mar. Geol.*, **271**, 3–4, 278–291.
- Orzech, M. D., A. J. H. M. Reniers, E. B. Thornton, and J. H. MacMahan (2011), Mega cusps on rip channel bathymetry: Observations and modeling, *Coastal Eng.*, doi:10.1016/j.coastaleng.2011.05.001.
- Puleo, J. A., R. A. Beach, R. A. Holman, and J. S. Allen (2000), Swash zone sediment suspension and transport and the importance of bore-generated turbulence, *J. Geophys. Res.*, **105**, 17021–17044.
- Reniers, A. J. H. M., J. A. Roelvink, and E. B. Thornton (2004), Morphodynamic modeling of an embayed beach under wave group forcing, *J. Geophys. Res.*, **109**, C01030.
- Richmond, B. M., and A. H. Sallenger (1984), Cross-shore transport of bimodal sands, *Proc. 19th Int. Conf. Coastal Eng.*, ASCE, 1997–2008.
- Roelvink, J. A., and M. J. F. Stive (1989), Bar generating cross-shore flow mechanisms on a beach, *J. Geophys. Res.*, **94** C4, 4485–4800.
- Roelvink, J. A., A. J. H. M. Reniers, A. R. van Dongeren, J. S. M. van Thiel de Vries, R. T. McCall, and J. Lescinski (2009), Modeling storm impacts on beaches, dunes and barrier islands, *Coastal Eng.*, **56** (11–12), 1133–1152.
- Roelvink, J. A., and A. J. H. M. Reniers (2011), *A Guide to Modeling Coastal Morphology. Advanced Series on Ocean Engineering*, World Scientific, Singapore, **12**, 292.
- Ruessink, B. G., Y. Kuriyama, A. J. H. M. Reniers, J. A. Roelvink, and D. J. R. Walstra (2007), Modeling cross-shore sandbar behavior on the timescale of weeks, *J. Geophys. Res.*, **112**, F03010.
- Shields, A. (1936), Anwendung der Aehnlichkeitsmechanik und Turbulenzforschung auf die Geshiebbewegung, Mitt Preuss Versuchsanstalt fur Wasserbau und Schiffbau, Berlin in German. **26**.
- Stauble, D. K., and M. A. Cialone (1997), Sediment dynamics and profile interactions: DUCK94, *Proc. 25th Int. Coastal Eng. Conf.*, 1–14.
- Swart, D. (1974), Offshore sediment transport and equilibrium beach profiles, *Tech. Rep.*, **131**, WL-Delft Hydraulics.
- Terrile, E., A. J. H. M. Reniers, and M. J. F. Stive (2009), Acceleration and skewness effects on the instantaneous bed shear stresses in shoaling waves, *J. Waterw. Port Coastal Ocean Eng.*, **135**, 228–234.
- Ting, F. C. K., and J. T. Kirby (1994), Observation of undertow and turbulence in a laboratory surf zone, *Coastal Eng.*, **24**, 51–80.
- Turner, I. L., and G. Masselink (1998), Swash infiltration-exfiltration and sediment transport, *J. Geophys. Res.*, **103**, 30,813–30,824.
- Van Rooijen, A. A., A. J. H. M. Reniers, J. S. M. van Thiel de Vries, C. E. Blenkinsopp, and R. T. McCall (2012), Modeling swash zone sediment transport at Truc Vert Beach, *Proc. Int. Conf. Coastal Eng.*, Santander, Spain.
- van Rooijen, A. A. (2011), Modelling sediment transport in the swash zone, MSc thesis, Delft University of Technology, 142.
- Voulgaris, G., and M. B. Collins (2000), Sediment resuspension on beaches: Response to breaking waves, *Mar. Geol.*, **167**, 167–187.
- Wiberg, P. L., D. E. Drake, and D. A. Cacchione (1994), Sediment resuspension and bed armoring during high bottom stress events on the northern California inner continental shelf: Measurements and predictions, *Cont. Shelf Res.*, **14**, 1191–1219.
- van Thiel de Vries, J. S. M., M. R. A. van Gent, D. J. R. Walstra, and A. J. H. M. Reniers (2008), Analysis of dune erosion processes in large-scale flume experiments, *Coastal Eng.*, **55**, 1028–1040.